Received: 30 January 2022 | Revised: 21 April 2022 | Accepted: 25 April 2022

DOI: 10.1096/fj.202200184RR

THE FASEB JOURNAL

RESEARCH ARTICLE

URMC-099 prophylaxis prevents hippocampal vascular vulnerability and synaptic damage in an orthopedic model of delirium superimposed on dementia

Patrick Miller-Rhodes[1,2] | **Herman Li**[1] | **Ravikanth Velagapudi**[3] | **Wesley Chiang**[4] | **Niccolò Terrando**[3,5,6] | **Harris A. Gelbard**[1,7,8,9,10]

[1]Center for Neurotherapeutics Discovery, Department of Neurology, University of Rochester Medical Center, Rochester, New York, USA

[2]Neuroscience Graduate Program, University of Rochester Medical Center, Rochester, New York, USA

[3]Department of Anesthesiology, Center for Translational Pain Medicine, Duke University Medical Center, Durham, North Carolina, USA

[4]Department of Biochemistry and Biophysics, University of Rochester Medical Center, Rochester, New York, USA

[5]Department of Cell Biology, Duke University Medical Center, Durham, North Carolina, USA

[6]Department of Immunology, Duke University Medical Center, Durham, North Carolina, USA

[7]Department of Neurology, University of Rochester Medical Center, Rochester, New York, USA

[8]Department of Neuroscience, University of Rochester Medical Center, Rochester, New York, USA

[9]Department of Pediatrics, University of Rochester Medical Center, Rochester, New York, USA

[10]Department of Microbiology & Immunology, University of Rochester Medical Center, Rochester, New York, USA

Correspondence
Niccolò Terrando, Department of Anesthesiology, Duke University Medical Center, Durham, NC, USA.
Email: niccolo.terrando@duke.edu

Funding information
NIA R01AG057525 (NT); NIH T32 GM135134 (WC).

Abstract

Systemic perturbations can drive a neuroimmune cascade after surgical trauma, including affecting the blood–brain barrier (BBB), activating microglia, and contributing to cognitive deficits such as delirium. Delirium superimposed on dementia (DSD) is a particularly debilitating complication that renders the brain further vulnerable to neuroinflammation and neurodegeneration, albeit these molecular mechanisms remain poorly understood. Here, we have used an orthopedic model of tibial fracture/fixation in APPSwDI/mNos2$^{-/-}$ AD (CVN-AD) mice to investigate relevant pathogenetic mechanisms underlying DSD. We conducted the present study in 6-month-old CVN-AD mice, an age at which we speculated amyloid-β pathology had not saturated BBB and neuroimmune functioning. We found that URMC-099, our brain-penetrant anti-inflammatory neuroprotective

Abbreviations: AD, Alzheimer's disease; Aβ, amyloid beta; BBB, blood-brain barrier; BEC, brain endothelial cells; C1q, complement component 1q; CAA, cerebral amyloid angiopathy; CD, cluster of differentiation; CNS, central nervous system; CVN-AD, APPSwDI/mNos2−/− AD mice; DSD, delirium superimposed on dementia; DG, dentate gyrus; DMSO, dimethylsulfoxide; Iba1, ionized calcium binding adaptor molecule 1; ICC, immunocytochemistry; IHC, immunohistochemistry; IR, immunoreactivity; IL-1β, interleukin-1β; LRRK2, leucine rich repeat kinase type 2; Ly6G, lymphocyte antigen 6 complex locus G6D; MafB, v-maf musculoaponeurotic fibrosarcoma oncogene homolog B; MLK3, mixed lineage kinase type 3; NVU, neurovascular unit; NET, neutrophil extracellular trap; PECAM-1, platelet endothelial cell adhesion molecule-1; POD, postoperative delirium; SLM, stratum lacunosum moleculare; TNF-α, tumor necrosis factor-α; VCAM-1, vascular cell adhesion molecule type 1.

Patrick Miller-Rhodes and Herman Li contributed equally to this work.

This is an open access article under the terms of the Creative Commons Attribution-NonCommercial-NoDerivs License, which permits use and distribution in any medium, provided the original work is properly cited, the use is non-commercial and no modifications or adaptations are made.
© 2022 The Authors. *The FASEB Journal* published by Wiley Periodicals LLC on behalf of Federation of American Societies for Experimental Biology

drug, prevented inflammatory endothelial activation, breakdown of the BBB, synapse loss, and microglial activation in our DSD model. Taken together, our data link post-surgical endothelial activation, microglial MafB immunoreactivity, and synapse loss as key substrates for DSD, all of which can be prevented by URMC-099.

KEYWORDS

blood–brain barrier, CVN-AD, delirium superimposed on dementia, leucine-rich repeat kinase type 2, microgliosis, mixed lineage kinase type 3, neuroinflammation, URMC-099, vascular cell adhesion molecule type 1

1 | INTRODUCTION

Delirium is a common neurologic complication frequently encountered after major surgery, such as cardiac and orthopedic, which can impact neurodegenerative processes and contribute to significant mortality and morbidity in older and frail patients.[1] Indeed, patients with Alzheimer's disease (AD) often require orthopedic surgery to repair a broken limb and become particularly vulnerable to complications, including postoperative delirium (POD), an acute state of cognitive impairment that develops in the hospital setting.[2–4] POD is associated with an increased 1-year mortality and a worsening of cognitive trajectories in patients with pre-existing neurodegeneration.[5,6] Despite the prevalence of POD in this population, the pathophysiology of delirium superimposed on dementia (DSD) remains poorly understood and without disease-modifying or prophylactic therapeutic interventions.

Vascular etiologies for cognitive impairment and dementia are a growing research interest, yet the impact of systemic stressors on the neurovascular unit (NVU) is far less established, especially in the context of perioperative complications. To better understand the putative impact of surgery on neurovascular and immunological sequelae, we have developed a model of DSD following tibial fracture and fixation in CVN-AD mice.[7] In the absence of surgical manipulation, the CVN-AD model displays age-dependent effects including amyloid-β accumulation,[8] cerebral amyloid angiopathy (CAA), tau phosphorylation,[8–10] microgliosis,[8] astrogliosis,[9] NVU dysfunction,[11] increased expression of complement components,[9] and neuronal degeneration.[10] In the CVN-AD model, signs of neuroinflammation, including astrogliosis and microgliosis, appear as early as 12 weeks of age, spatial cognitive deficits as early as 24 weeks of age, and neurodegeneration as early as 36 weeks of age.[8] In our prior work, we have established that tibial fracture/fixation worsens the neuroinflammatory, neurodegenerative, and cognitive sequelae observed in 12-month-old, but not 3-month-old, CVN-AD mice.[7] These sequelae amyloid-β accumulation in the dentate gyrus (DG) region of hippocampus, delirium-like behavior as defined by inattention deficits in the 5-choice serial reaction time task, dramatic loss of AQP4, and concomitant fibrinogen deposition.[7] Since vascular factors, including vascular cell adhesion molecule type 1 (VCAM-1), have been identified in a proteomics screen as key gateway proteins associated with pathologic aging,[12] we sought to investigate whether surgery impacted VCAM-1 expression and other correlates of neurovascular vulnerability in DSD.

URMC-099 is a 7-azaindole-based MLK3 inhibitor that was developed using proprietary libraries for kinase drug design and a cell-free assay system described in Goodfellow et al. to identify potent MLK3 inhibitors with favorable pharmacokinetics and CNS penetrance.[13] URMC-099 potently inhibits a wide variety of kinases with roles in neurodegenerative disease, including MLK3, LRRK2, and MAP4K4. URMC-099 has proven effective in mouse models of multiple sclerosis,[14] AD,[15,16] and inflammatory conditions such as nonalcoholic steatohepatitis.[17] We and others have shown that genetic ablation of MLK3, LRRK2, or MAP4K4 is therapeutic in a variety of inflammatory and neurodegenerative conditions,[17–19] including orthopedic surgery model of delirium.[20]

Here, we test the hypothesis that URMC-099 prophylaxis prevents damage to the blood–brain barrier (BBB) and hippocampal synapses resulting from orthopedic surgery in 6- and 12-month-old CVN-AD mice, the former representing an early stage in AD progression and the latter late-stage disease.

2 | MATERIALS AND METHODS

2.1 | URMC-099

URMC-099 (M.W. 421) was synthesized as originally described in Goodfellow et al.[13] URMC-099 drug solutions were prepared by dissolving 20 mg of URMC-099 in 0.5-ml sterile dimethyl sulfoxide (DMSO; D8779,

Sigma-Aldrich, St. Louis, MO). We then added 4-ml polyethylene glycol 400 (PEG400; 91893-250-F, Sigma-Aldrich) and 5.5-ml sterile saline (National Drug Code NDC0409-4888-10) for a final concentration was 2-mg/ml URMC-099. The vehicle was the same solution minus URMC-099. Mice were administered (i.p.) three injections of URMC-099 (10 mg/kg) at 12-h intervals prior to orthopedic surgery with the last dose being immediately prior to surgery. The volume of URMC-099/vehicle administered was titrated based off body weight (5 ml/kg; e.g., 0.1 ml/20 g body weight). Drug solutions were coded such that experimenters were blinded to the experimental conditions for the duration of the experiments.

2.2 | Cell culture

Bend.3 cells[21] (ATCC CRL-2299; BALB/c origin; generously provided by Dr. Ning Quan) were cultured in glutamate-free Dulbecco's Modified Eagle's Medium (DMEM) supplemented with GlutaMAX (1% v/v) and fetal bovine serum (FBS; 10% v/v) and maintained in a humidified 37°C incubator (5% CO_2). For immunocytochemistry (ICC), bend.3 cells were seeded at a density of 100 000 cells per well on plasma-cleaned, poly-D-lysine-coated coverslips in a 12-well plate and allowed to adhere overnight. Subsequently, bend.3 cells were serum starved for 30 min, followed by addition of URMC-099 (300 nM in DMSO). Thirty minutes after URMC-099 pretreatment, PBS or IL-1β (10 ng/ml, a dose informed by Ref. [12]) was added as indicated. Bend.3 cells were fixed 16 h post-IL-1β stimulation for ICC. For quantitative reverse-transcriptase polymerase chain reaction (qRT-PCR), bend.3 cells were treated exactly as above, except cells were seeded at 200 000 cells per 12-well plate and lysates were collected at 6 h post-IL-1β stimulation. Because biological reproducibility cannot be measured in cell lines, all cell line experiments were performed once, with all values and statistics computed across replicate wells.

2.3 | Resazurin assay

Cell viability was assayed using an alamarBlue (Thermo Scientific; cat# 88952) resazurin metabolism fluorescent assay. After the cells reached >90% confluency, the cells were primed for treatment in a reduced serum media (DMEM + 1% FBS) for 3 h. URMC-099 (300 nM in DMSO), IL-1β (10 ng/ml), or their respective controls were added along with the alamarBlue reagent at a final concentration of 10% v/v. After 15 h, a spectrophotometer plate reader (λ_{ex} = 550 nm, λ_{em} = 590 nm) was used to assess the degree of resazurin metabolism in each treatment group. Blank wells containing only 10% v/v alamarBlue in the reduced serum media were used to correct for baseline fluorescence. Viability measurements were conducted over two passages.

2.4 | Animals and orthopedic surgery

APPSwDI/mNos2$^{-/-}$ AD mice (CVN-AD; kindly provided by Dr. Carol Colton, Duke University) were bred and maintained by the Terrando laboratory at Duke University. The procedures followed to provide tissues from APPSwDI/mNos2$^{-/-}$ AD mice were performed in strict compliance with animal protocols approved by the Institutional Animal Care and Use Committees (IACUC) of Duke University (A249-17-11). Mice were housed under a 12-h light/dark cycle with free access to water and regular chow. URMC-099 prophylaxis and orthopedic surgery were performed as described in Miller-Rhodes et al.[20] on 6- and 12-month APPSwDI/mNos2$^{-/-}$ mice under isoflurane (Patterson Veterinary, Greeley, CO) anesthesia and analgesia (buprenorphine, 0.1 mg/kg subcutaneously; ZooPharm, Laramie, WY). Briefly, a small incision was performed on the shaft of the tibia followed by muscle disassociation and stripping of the periosteum. Pinning of the tibia was performed by inserting a 0.38-mm stainless steel rod and osteotomy was performed on the upper crest of the bone. All mice recovered from surgery and were included in the study.

2.5 | Immunocytochemistry

Immunocytochemistry was performed per Glynn et al.'s protocol[22] with minor modifications. Briefly, following fixation in 4% PFA/4% sucrose solution for 15 min at 4°C, cells were washed with 100 nM glycine (in 1X PBS), followed by two more washes in 1X PBS. Cells were permeabilized in 0.25% Triton-X for 5 min (followed by two PBS washes), blocked in 10% bovine serum albumin (BSA) in 1X PBS, and incubated with primary antibodies in 3% BSA for 1 h at room temperature. Primary antibodies included rat monoclonal anti-VCAM1 (Abcam, ab19569, clone M/K-2; 1:250) and Armenian hamster anti-PECAM-1 (CD31; Millipore Sigma, cat no. MAB1398Z, clone 2H8; 1:250). Cells were washed again three times with 1X PBS and incubated with secondary antibodies in 3% BSA for 45 min at room temperature. Cells were washed a final three times with 1X PBS, dipped in ddH20 to remove excess salt, and mounted on microscope slides with Prolong Diamond anti-fade reagent (ThermoFisher, cat no. P36961).

2.6 | Quantitative reverse transcriptase polymerase chain reaction (qRT-PCR)

RNA was extracted using a spin column RNA isolation kit (Machery-Nagel). On-column DNase treatment was used to remove contaminating genomic DNA. Total RNA preparations were then used directly for qPCR (200 ng total RNA per reaction) using the Luna Universal One-Step RT-qPCR Kit (NEB, E3006) and target-specific primer/probe sets (ThermoFisher) or frozen at −80°C until use. The qPCR primer/probe sets we used include the endogenous control *Ipo8* (Mm01255158_m1), *Vcam1* (Mm01320970_m1), *Spp1* (Mm00436767_m1), *Timp1* (Mm01341361_m1), and *Col1a1* (Mm00801666_g1). The ΔΔ*Ct* method was used to analyze the results.

2.7 | Immunohistochemistry

Twenty-four hours after orthopedic surgery, mice were deeply anesthetized with isoflurane and transcardially perfused with PBS and subsequently 4% PFA. Brains were carefully extracted and post-fixed for 24 h in 4% PFA. Brains were transferred to conical tubes containing PBS, packed with ice packs, and shipped to the Gelbard laboratory at the University of Rochester Medical Center. Free-floating coronal brain sections (40-μm thickness) were cut using a vibratome and stored in cryoprotectant (30% PEG300, 30% glycerol, 20% 0.1 M phosphate buffer, and 20% ddH_2O) at −20°C. For immunohistochemistry, cryopreserved sections were washed three times in 1X PBS followed by another wash in 0.1 M glycine in 1X PBS (to reduce autofluorescence). Sections were subsequently incubated in blocking buffer (1.5% BSA, 3% normal goat serum, 0.5% Triton-X, and 1.8% NaCl in 1X PBS) containing primary antibodies (VCAM1 Millipore Sigma MAB1398Z 1:200; Tmem119 SySy 1:500; Iba1 Wako PTR2404 1:1000; MafB Atlas HPA005653 1:500; CD68 Serotec MCA1957GA 1:1000; Homer1 SySy 160006 1:500; PSD95 NeuroMab 75-028 1:500; Piccolo SySy 142104 1:500; C1q Abcam AB71940 1:500; CD31 Millipore Sigma MAB1398Z 1:250; Fibrinogen Dako A0080 1:200; H3Cit Abcam ab5103 1:500) in blocking buffer (1.5% BSA, 3% normal goat serum, 0.5% Triton-X, and 1.8% NaCl in 1X PBS) overnight at room temperature. Then, sections were washed thrice in 1X PBS containing 1.8% NaCl before incubating in Alexa Fluor conjugated secondary antibodies (ThermoFisher), again overnight. Finally, sections were washed three times with 1X PBS+1.8% NaCl, mounted on glass slides, and cover-slipped with Prolong Diamond Antifade Reagent (Invitrogen P36961). When used, the UV-excitable fibrillar amyloid-β dye Amylo-Glo (Biosensis TR-300-AG; 1:100) or Alexa-633 Hydrazide (Thermo Fisher A30634; 1:1000) was diluted in 1X PBS+1.8% NaCl and applied to sections for 10 min following the first two post-secondary washes; an additional two washes (1X PBS+1.8% NaCl) were performed to rinse the sections of excess Amylo-Glo dye or Alexa-633 Hydrazide.

2.8 | Grid pseudo-confocal microscopy and image analysis

Slides were coded throughout imaging and analysis to reduce experimenter bias. We used an Olympus BX-51 microscope equipped with Quioptic Optigrid hardware (for optical sectioning) and a Hamamatsu ORCA-ER camera. Images were acquired using Volocity 3DM software (Quorum Technologies). Within each set, light intensity and exposure settings were kept constant. For ICC, three images were acquired for each experimental replicate. For IHC, six images were acquired for each biological replicate. Synaptic punctae were imaged at 60× magnification (10 μm depth, 0.3 μm step size). To reduce variability due to differences in vascular coverage (i.e., areas without synaptic punctae), we selected 300 × 300 pixel ROIs from each XYZ-stack for analysis. Other markers were imaged at 20× and 40× magnification. Immunostained objects were identified and quantified using custom Volocity workflows. More specifically, for synaptic punctae, the colocalization of spots and objects were used to identify punctae. The "Find Spots" function was used to identify individual puncta based on local intensity maxima and "Find Objects" function was used to identify punctae with a minimum intensity threshold; all other quantified objects were identified using the "Find Objects" function. Arterial VCAM-1 vessels were defined as VCAM-1 objects touching Alexa-633 objects. Tmem119^{lo} and Tmem119^{hi} Iba1-positive cells were determined by intensity thresholding (by standard deviation; SD = 1.2). Microglial MafB intensity was quantified as the sum intensity of MafB objects contained within Iba1-positive objects and normalized to the number of microglia in each field of view. Nonmicroglial MafB was quantified as the sum intensity of MafB objects *not* contained within Iba1-positive objects and normalized to the number of MafB+ nuclei per field. Microglial CD68 was quantified as the sum intensity of CD68 objects contained with Iba1-positive objects. Extravascular fibrinogen quantified as fibrinogen object intensity not colocalized with CD31.

2.9 | Statistics

All qPCR statistics were performed on ΔCt values and then represented graphically as fold change ($2^{-\Delta\Delta Ct}$).

One- and two-way analyses of variance (ANOVAs) with Holm-Sidak's or Tukey's multiple comparison tests were used to analyze the ICC and IHC data as indicated in each figure legend. Pearson's correlation was used to compute correlations between VCAM-1 immunoreactivity and fibrillar amyloid-β volume. All data are presented as mean ± standard error (SEM) with significance at $p < .05$.

3 | RESULTS

3.1 | Effect of URMC-099 on brain endothelial cell activation in vitro

Although URMC-099's pharmacokinetic properties allow it to readily cross the BBB and achieve therapeutic concentrations in the CNS to act directly on microglia, its therapeutic efficacy in *in vivo* models of systemic inflammation may be attributable, at least in part, to actions on the cerebrovascular endothelium. To test whether URMC-099 can inhibit the activation of brain endothelial cells (BECs) under inflammatory conditions, we analyzed VCAM-1 and PECAM-1 (CD31) immunoreactivity (IR) on bend.3 cells, a murine cerebral microvascular endothelial cell line,[21] following stimulation with the pro-inflammatory cytokine IL-1β (10 ng/ml, as previously used in Ref. [12]) alone or in combination with URMC-099 (300 nM). Twenty-four hours following IL-1β stimulation, bend.3 cells upregulated VCAM-1 ($p = .0268$), but not PECAM-1 immunoreactivity (Figure 1A–C). URMC-099 pretreatment virtually abolished the IL-1β-induced increase in VCAM-1 immunoreactivity ($p < .0141$; Figure 1A,B). Additionally, it also reduced the basal immunoreactivity of PECAM-1 by 24% after IL-1β stimulation but failed to reach significance ($p = .186$; Figure 1A,C). We next characterized the effect of URMC-099 on the transcriptional response of bend.3 cells to IL-1β. In addition to *Vcam1*, we assayed the expression of *Spp1*, *Timp1*, and *Col1a1*—all of which are upregulated in activated BECs *in vivo* in murine disease models of core BBB dysfunction.[23] We focused on *Spp1*, *Timp1,* and *Col1a1* because of their respective roles in BBB repair following injury,[24] preserving BBB integrity,[25] and functional integrity of extracellular matrix proteins,[26] respectively. IL-1β upregulated *Vcam1* expression 59.16-fold ($p < .0001$) and elicited smaller (<2-fold) increases in *Spp1* ($p = .0002$) and *Timp1* ($p = .0004$) mRNA (Figure 1D). Of these genes, URMC-099 pretreatment significantly reduced *Vcam1* ($p < .0001$) and *Spp1* ($p = .0008$) mRNA levels (Figure 1D). In addition, IL-1β decreased the expression of *Col1a1* by 25% versus control ($p = .0077$), an effect that was not modulated by URMC-099 pretreatment (Figure 1D). Changes observed due to URMC-099 and/or IL-1β were independent of viability (Figure 1E). Together, these experiments demonstrate that URMC-099 exerts anti-inflammatory effects on BEC activation in vitro.

3.2 | URMC-099 prophylaxis inhibits cerebrovascular VCAM-1 immunoreactivity after orthopedic surgery in CVN-AD mice

Based on our in vitro BEC results, we hypothesized that URMC-099 prophylaxis would inhibit cerebrovascular inflammation in the stratum lacunosum moleculare (SLM) of CVN-AD mice following surgery. We focused on the SLM because it is a hippocampal subregion that has been implicated in AD and delirium.[27,28] Orthopedic surgery elicited a 1.7-fold increase in total VCAM-1 volume in the SLM relative to naïve, vehicle-treated controls (18 542.5 ± 2318.7 μm^3 vs. vehicle-treated controls 10 840.8 ± 2825.2 μm^3; $p < .0001$; Figure 2A–D,E). In agreement with our in vitro data, URMC-099 prophylaxis decreased total VCAM-1 in the SLM (12 679.7 ± 1698.5 μm^3; $p = .0006$; Figure 2E). To determine whether these effects were specific to arterial or venous BECs, we used the arterial-specific dye Alexa 633 hydrazide[29]—which binds to elastin fibers present in arterioles—to distinguish between arterial and venous VCAM-1 objects in our analysis. Arterial VCAM-1 accounted for 27.3% of total VCAM-1 volume; furthermore, there were no main effects of surgery [$F(1, 20) = 3.53$; $p = .08$] nor URMC-099 treatment [$F(1, 20) = 0.22$; $p = .65$] on arterial VCAM-1 levels (Figure 2A′–D′,E). In contrast, we observed significant main effects of surgery [$F(1, 20) = 15.27$; $p = .0009$] and URMC-099 [$F(1, 20) = 14.32$; $p = .0012$] on venous VCAM-1 levels, mirroring the differences between groups observed in total VCAM-1 volume. In order to eliminate the possibility of more vessels as a contributor of increased VCAM-1 volume, we assessed VCAM-1 mean fluorescence as a measure of fluorescent intensity normalized to its volume. Mean VCAM-1 fluorescent intensity has been shown to be aberrant in other vasculopathy states such as diabetic retinopathy.[30] In our model, PECAM-1 was found to be inadequate to assess total vascular volume as its expression changed following surgical trauma. In addition, tomato-lectin was found to significantly co-stain more microglia that vasculature, thus not offering a reliable quantification in the blood vessels (data not shown). We found orthopedic surgery induced a 47% increase in VCAM-1 density compared to sham mice (5873.6 ± 425.2 a.u./μm^3 vs. sham 3993.9 ± 108.4 a.u./μm^3; $p < .001$; Figure 2F). Furthermore, pretreatment of URMC-099 prevented VCAM-1 induction in mice that received orthopedic surgery compared to vehicle-treated

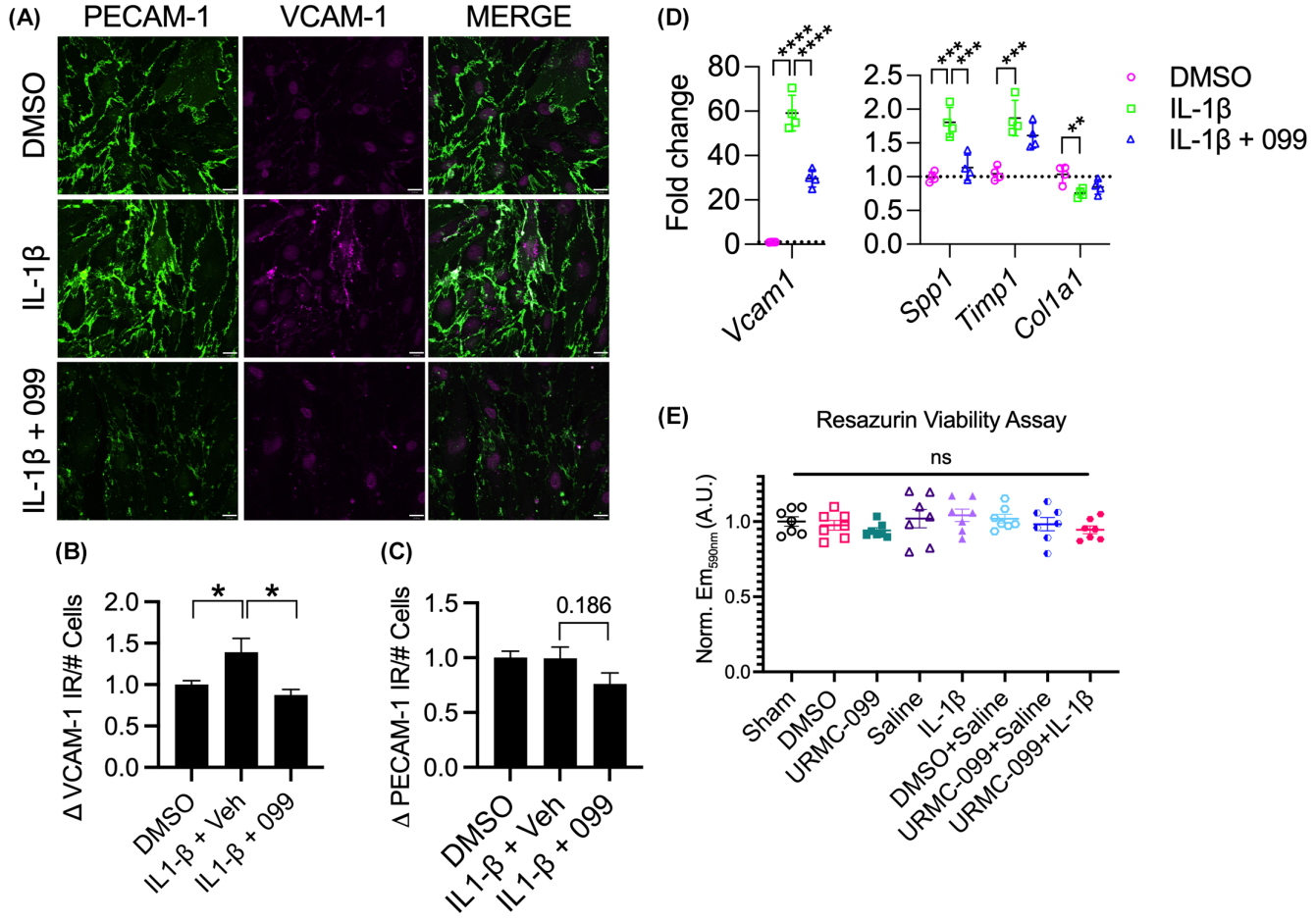

FIGURE 1 URMC-099 inhibits BEC activation in vitro. Serum-deprived bend.3 cells were pretreated with URMC-099 (099) or DMSO for 30 min, after which cells were stimulated with IL-1β (10 ng/ml). (A) Representative images of VCAM-1 and PECAM-1 staining in bend.3 cells; scale bar = 15 μm. (B) Quantification of PECAM-1 immunoreactivity (IR) normalized to the number of cells, represented as fold change. (C) Quantification of VCAM-1 immunoreactivity normalized to the number of cells, represented as fold change. (D) qPCR analysis of bend.3 transcriptional response to IL-1β and URMC-099 treatment. (E) Quantification of Resazurin Viability fluorescence, represented as fold change to blank controls ($N = 7$ cell culture wells). Values presented as mean ± SEM ($N = 4$ cell culture wells). $^{**}p < .01$, $^{***}p < .001$, $^{****}p < .0001$ for indicated comparisons; one-way ANOVA with Dunnett's multiple comparison test (B–D)

mice (4949.8 ± 275.6 a.u./μm^3; $p < .05$; Figure 2F). To rule out a potential contribution of Aβ burden on cerebrovascular VCAM-1 levels, we visualized fibrillar Aβ in the SLM using the UV dye Amylo-Glo (Figure 2A–D). We did not detect significant differences in fibrillar Aβ between any experimental condition (Figure 2G), nor was there any correlation between fibrillar Aβ levels and total VCAM-1 levels in the SLM (Figure 2H). Overall, these results indicate that URMC's effect is to reduce capillary and venular VCAM-1 levels in the SLM. These

FIGURE 2 URMC-099 prophylaxis prevents the induction of VCAM-1 in the SLM of 6-month-old CVN-AD mice following surgery. Six- and twelve-month-old CVN-AD mice ($N = 6$/group) received three doses i.p. of URMC-099 (10 mg/kg) prior to undergoing sham or orthopedic surgery. Brains were harvested 24 h post-surgery for IHC. (A–D) Representative images depicting VCAM-1 (green) and fibrillar AB (cyan). (A′–D′) Representative images depicting arterial VCAM-1 vessels using the artery-specific dye Alexa 633-hydrazide (magenta); images correspond to experimental conditions represented by A–D; scale bar = 32 μm. (E) Quantification of VCAM-1 volume venous VCAM-1 volume (white bars) and arterial VCAM-1 volume (blue bars) at 6 months of age. (F) Quantification of VCAM-1 intensity normalized to volume at 6 months of age. (G) Quantification of fibrillar AB. (H) Correlation between total VCAM-1 volume and fibrillar AB volume at 6 months of age. (I) Quantification of total VCAM-1 volume (full bars), venous VCAM-1 volume (white bars), and arterial VCAM-1 volume (blue bars) at 12 months of age; statistical comparisons are shown for total VCAM-1. (J) Quantification of VCAM-1 intensity normalized to volume at 12 months of age. Values presented as mean ± SEM ($N = 6$); $^{*}p < .05$, $^{***}p < .001$, $^{****}p < .0001$ for indicated comparisons; two-way ANOVA with Holm-Sidak's multiple comparison test (E,F) or Pearson's coefficient (D)

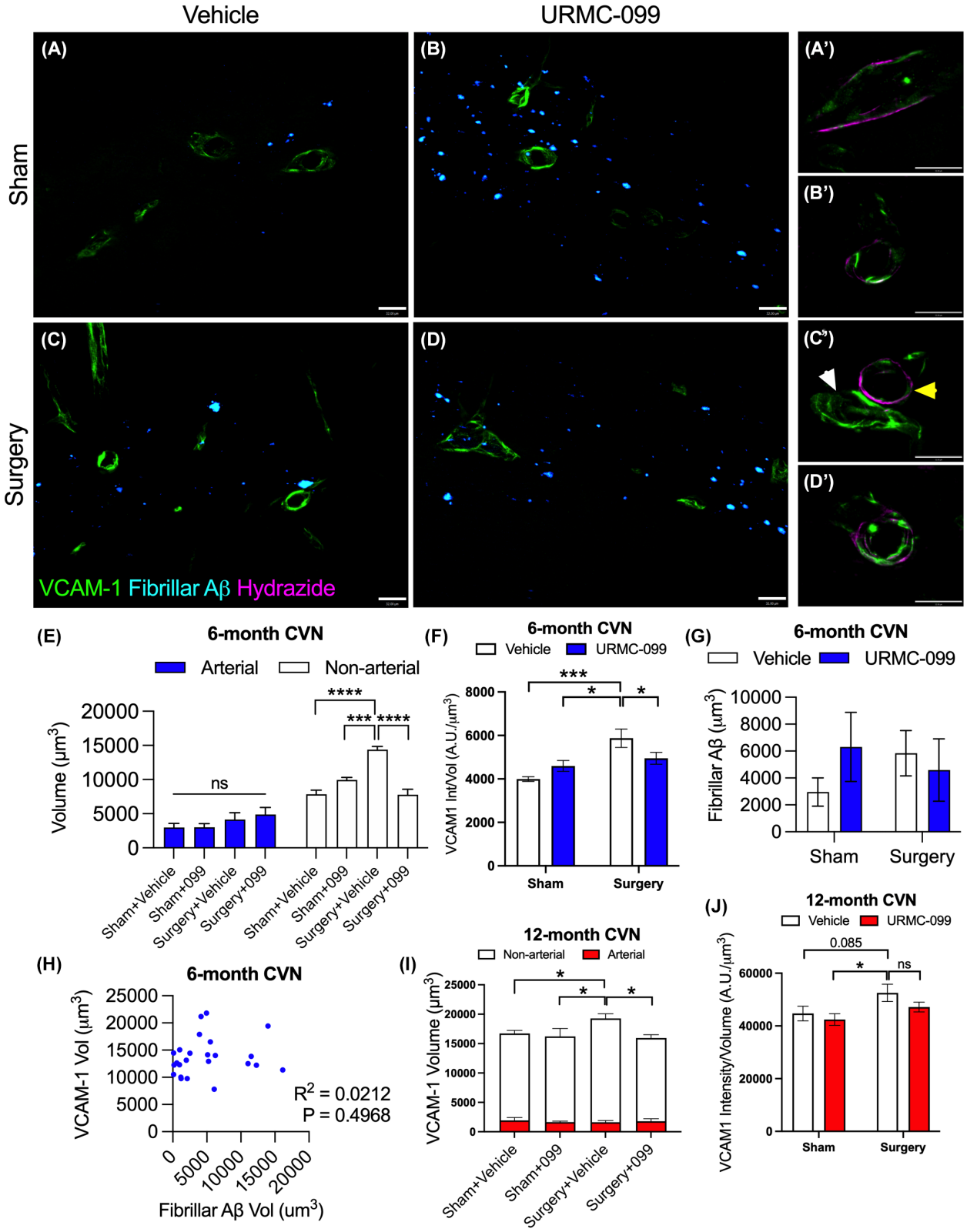

data further suggest that therapeutic intervention earlier in the course of neuropathogenesis may elicit better outcomes in this DSD model. In support of this interpretation, experiments in 12-month-old CVN mice demonstrated advanced pathology in hippocampal SLM with limited efficacy by URMC-099 in the late stages of the disease (Figure 2I,J).

3.3 | URMC-099 prophylaxis prevents vascular neutrophil NET formation and barrier dysfunction after orthopedic surgery in CVN-AD mice

To further evaluate barrier dysfunction in CVN-AD mice after surgery, we measured fibrinogen

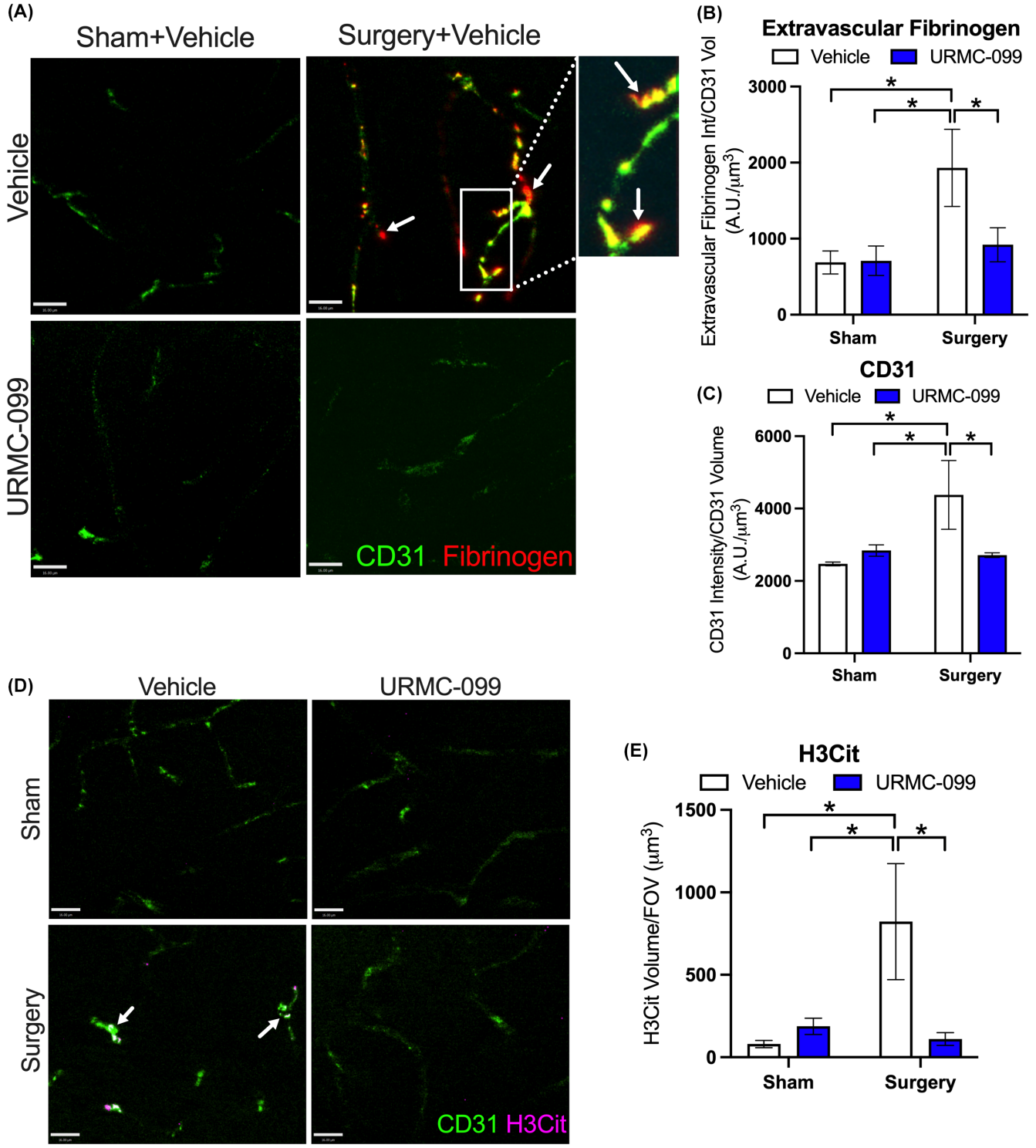

FIGURE 3 URMC-099 prevents vascular damage in the SLM of 6-month-old CVN-AD mice following orthopedic surgery. Six-month-old CVN-AD mice ($N = 6$/group) received three doses i.p. of URMC-099 (10 mg/kg) prior to undergoing sham or orthopedic surgery. Brains were harvested 24 h post-surgery for IHC. (A) Representative images depicting CD31/Pecam1 (green) and fibrinogen (red) with arrows being sites of fibrinogen leak; scale bar = 16 μm. (B) Quantification of extravascular fibrinogen. (C) Quantification of CD31/Pecam1 intensity normalized to CD31/Pecam1 volume. (D) Representative images depicting CD31/Pecam-1 (green) and NET marker, H3Cit (magenta) with arrows being sites of colocalization; scale bar = 16 μm. (E) Quantification of neutrophil NET marker, H3Cit. Values presented as mean ± SEM ($N = 6$); *$p < .05$ for indicated comparisons; two-way ANOVA with Holm-Sidak's multiple comparison test (C–E)

extravasation out of CD31+ vessels in the SLM at 24 h (Figure 3A). Surgery induced a robust 2.8-fold increase of fibrinogen out of the vascular lumen compared to naïve vehicle-treated controls (1931.4 ± 508.4 μm^3 vs. sham 687.6 ± 105.7 μm^3; $p < .05$), which was effectively prevented by URMC-099 (920.110 ± 224.1 μm^3; $p < .05$; Figure 3B) with arrows being sites of fibrinogen leakage outside of the lumen. Extravascular fibrinogen deposition was co-localized with an induction of CD31 expression (Figure 3C), further highlighting the key role of neurovascular damage in this model of DSD. To assess the contribution of neutrophils to barrier dysfunction, we measured the formation of neutrophil extracellular traps (NETs) using citrullinated histone H3 (H3Cit) a hallmark of NETs. Interestingly, we found orthopedic surgery caused significant 10.2-fold increase of NETs along the vascular lumen in the SLM (822.7 ± 351.7 μm^3 vs. vehicle-treated sham 80.1 ± 22.2 μm^3; $p < .05$; Figure 3D,E). Formation of perivascular NETs was prevented with pretreatment of URMC-099 compared to vehicle-treated surgical mice (110.2 ± 38.8 μm^3; $p < .05$; Figure 3D,E). Interestingly, histological assays did not show any visible Ly6G+ neutrophils in the SLM (data not shown).

3.4 | URMC-099 prophylaxis ameliorates synapse loss following orthopedic surgery in CVN-AD mice

Mouse models of POD and AD feature synaptic dysfunction and loss as pathological correlates of cognitive decline.[31–33] To this end, we quantified synaptic punctae corresponding to pre- (Piccolo) and post-synaptic (Homer1, PSD95) elements in the SLM of mice 24 h post-surgery (Figure 4). Surgery reduced Piccolo+ synaptic punctae by 33% ($p = .011$; Figure 4A,C), and Homer1+ and PSD95+ postsynaptic punctae by 10%–14% ($p = .023$ and $p = .046$, respectively; Figure 4A,B,D,E) relative to naïve controls. URMC-099 pretreatment prevented loss of Piccolo+, PSD95+, and Homer1+ punctae comparable to control levels.

3.5 | URMC-099 prophylaxis prevents the induction of MafB in microglia following orthopedic surgery in CVN-AD mice

Lineage-specific transcription factors have recently been shown to regulate pathological microglial states under neurodegenerative and inflammatory conditions.[34,35] In particular, the transcription factor MafB was shown recently to drive activation of spinal cord microglia in a mouse model of neuropathic pain.[35] Furthermore, we have recently demonstrated that basal levels of MafB in microglial cells are dependent on availability of lipids in the extracellular milieu either from serum or from apoptotic debris of dying microglial cells.[36] Not only are apoptotic cells rich sources of lipids, so too are synapses.[37] Thus, we hypothesized that the neurodegenerative sequelae observed in our DSD model might also drive the upregulation of microglial MafB as a marker of microgliosis. To this end, we evaluated the levels of the transcription factor MafB in SLM microglia following surgery and URMC-099 prophylaxis in CVN-AD mice. We visualized microglia using the pan-macrophage marker Iba1 and the microglia-specific marker Tmem119[38]; only Iba1 cells co-labelled with Tmem119 were defined as microglia. $Tmem119^{hi}$ cells accounted for >95% of Iba1+ cells in our image set the rest expressing Tmem119 at low levels (Figure S1A,B). We observed no effects due to surgery [$F(1, 20) = 0.748$; $p = .397$] and treatment with URMC-099 [$F(1, 20) = 0.789$; $p = .384$] on counts of Iba1+$Tmem119^{hi}$ and Iba1+$Tmem119^{lo}$ cells (Figure S1B). Orthopedic surgery increased the mean MafB immunoreactivity per cell in SLM microglia ($p = .011$), an effect that was abrogated by URMC-099 prophylaxis ($p = .046$; Figure 5A–C). MafB induction in SLM microglia appeared homogenous in our frequency histogram analysis (Figure 5C). Overall, URMC-099 prevented the effect of surgery on microglial MafB induction. MafB is expressed in other CNS cell types, namely neurons.[35,39,40] To determine whether the induction of MafB was limited to microglia, we quantified the expression of nonmicroglial MafB immunoreactivity (i.e., $Iba1^-$ MafB objects). We observed no main effects of surgery [$F(1, 20) = 0.9857$; $p = .3326$] nor URMC-099 treatment [$F(1, 20) = 1.266$; $p = .2738$] on nonmicroglial MafB immunoreactivity (Figure S2). These results indicate the microglial MafB, but not neuronal MafB, is increased following orthopedic surgery in CVN-AD mice.

3.6 | Orthopedic surgery and URMC-099 do not affect C1q deposition and microglial CD68/Iba1 immunoreactivity in CVN-AD mice

The opsonin C1q mediates microglia-dependent synapse loss in diverse contexts[32,41] and is transcriptionally regulated by MafB.[42] These observations raise the possibility that microglia eliminate synapses via increased C1q deposition following orthopedic surgery. Although C1q expression was very robust throughout the SLM (Figure 6A), in agreement with previous findings by Stephan et al.,[43] we observed no effects of surgery [$F(1, 20) = 0.4938$; $p = .4903$]

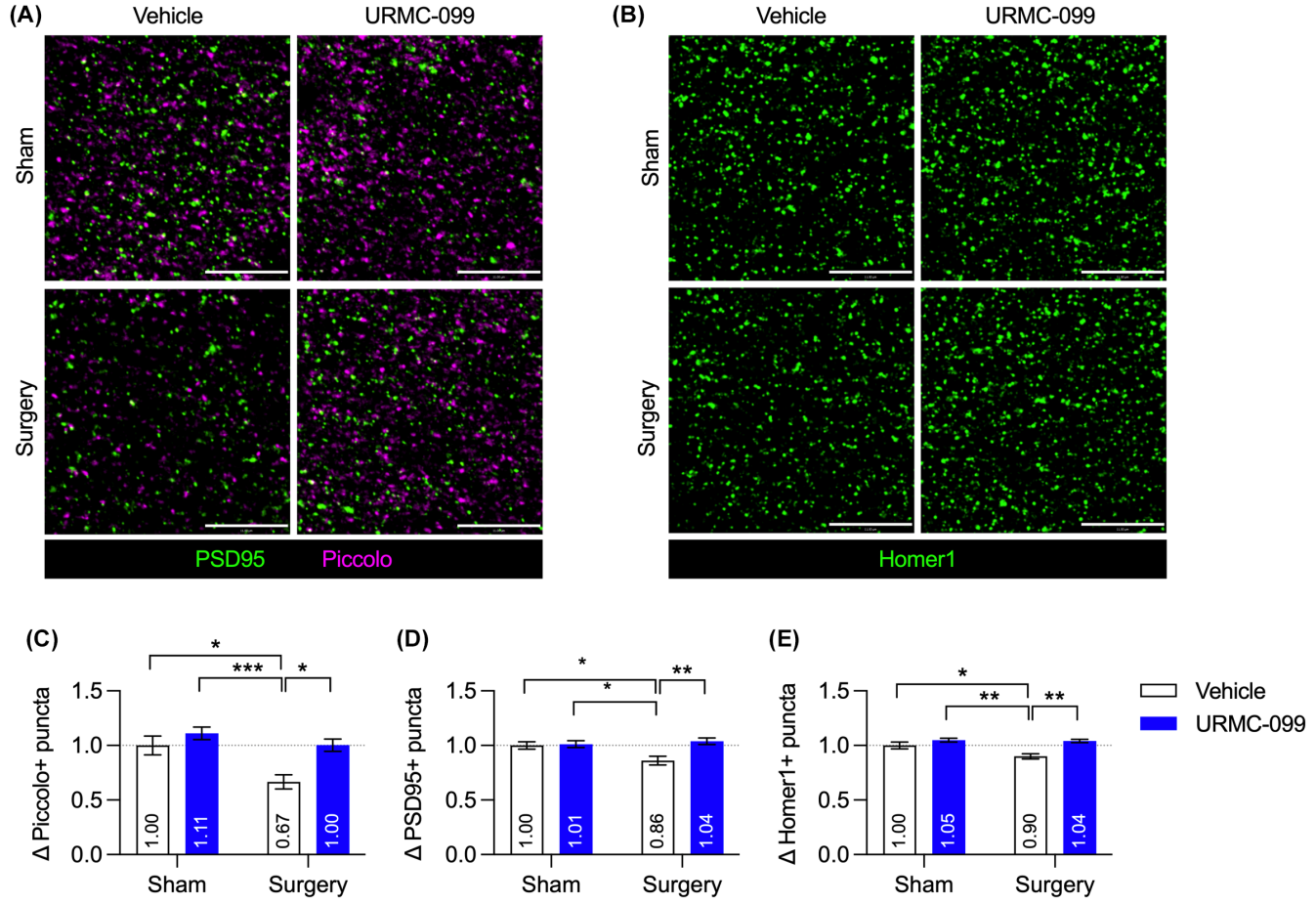

FIGURE 4 URMC-099 prevents synapse loss in the SLM of CVN-AD mice following orthopedic surgery. Six-month-old CVN-AD mice ($N = 6$/group) received three doses i.p. of URMC-099 (10 mg/kg) prior to undergoing sham or orthopedic surgery. Brains were harvested 24 h post-surgery for IHC. (A) Representative ROIs depicting PSD95+ (postsynaptic) and Piccolo+ (presynaptic) puncta; scale bar = 11 μm. (B) Representative ROIs depicting Homer1+ (postsynaptic) puncta; scale bar = 11 μm. (C) Quantification of presynaptic Piccolo+ puncta, represented as fold change. (D) Quantification of postsynaptic PSD95+ puncta, represented as fold change. (E) Quantification of postsynaptic Homer1+ puncta, represented as fold change. Values presented as mean ± SEM ($N = 6$); *$p < .05$, **$p < .01$, ***$p < .001$ for indicated comparisons; two-way ANOVA with Holm-Sidak's multiple comparison test (C–E)

nor URMC-099 treatment [$F(1, 20) = 0.0280$; $p = .8689$] on C1q deposition (Figure 6B). We next quantified the lysosomal marker CD68, whose expression is associated with activated phagocytic microglia[44] in Iba1+ cells in the SLM. However, these cells in the SLM contained high levels of CD68 regardless of condition; but neither orthopedic surgery [$F(1, 20) = 0.8440$; $p = .3692$] nor URMC-099 treatment [$F(1, 20) = 0.8440$; $p = .3692$] altered CD68 levels in Iba1+ cells (Figure 6C). We then quantified changes in microglia activation utilizing the pan-myeloid marker, Iba1. Although not well understood, during microgliosis expression of Iba1 is increased along with a thickening of processes. After surgery, we found there is a positive trend of Iba1 expression along with a negative trend in surface area compared to sham ($p = .0511$ and $p = .0921$, respectively; Figure 6C,D). Taken together, these results demonstrate that C1q, in contrast to its roles during brain development and models of AD,[32,41] does not participate in microglial phagocytosis of synapses in this orthopedic model of DSD.

Based on our results in this model of DSD, we have summarized URMC-099's different sites of action in a visual abstract (Figure 7). Overall, in CVN-AD mice receiving orthopedic surgery, URMC-099 prophylaxis exerts therapeutic effects—including reduced endothelial VCAM-1 expression, neurovascular damage, and synaptic loss.

4 | DISCUSSION

Here, we show that URMC-099 prophylaxis is effective in the CVN-AD mouse model of DSD *prior* to the onset of age-dependent progressive vascular injury by mitigating brain endothelial cell activation (i.e., VCAM-1 and CD31 induction), vascular damage (fibrinogen leak and NET

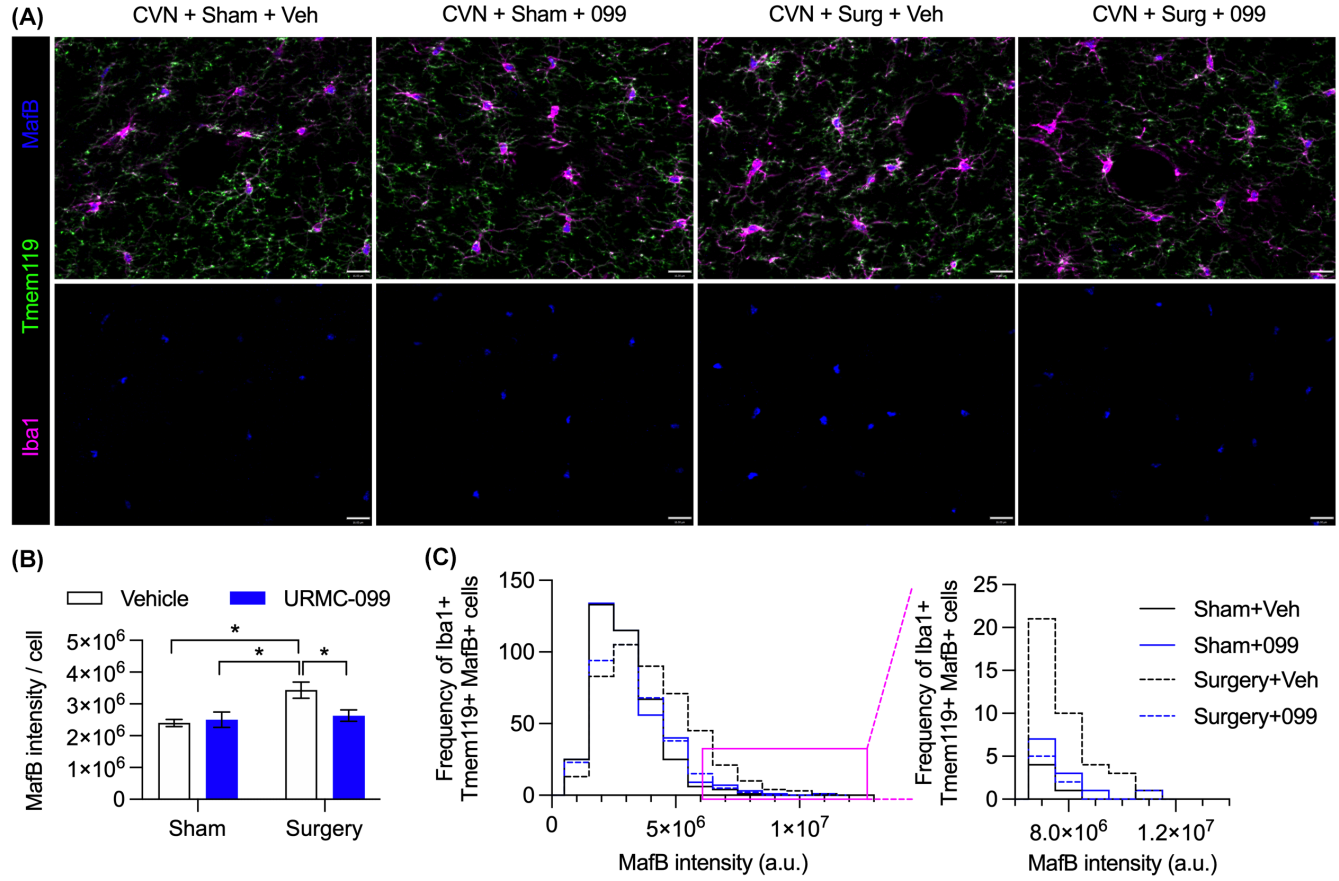

FIGURE 5 URMC-099 prevents changes in MafB microglial expression in the SLM of CVN-AD mice following orthopedic surgery. Six-month-old CVN-AD mice ($N = 6$/group) received three doses i.p. of URMC-099 (10 mg/kg) prior to undergoing sham or orthopedic surgery. Brains were harvested 24 h post-surgery for IHC. (A) Representative images depicting the pan-macrophage marker Iba1 (magenta), the microglia-specific marker Tmem119 (green), and the transcription factor MafB (blue); scale bar = 16 μm. (B) Quantification of mean MafB intensity per microglia. (C) Frequency histogram showing the number of microglia per MafB intensity bin (bin size = 1.0×10^6 a.u.). (C, inset) Frequency histogram depicting cell frequencies with high MafB intensity. Values presented as mean ± SEM ($N = 6$); *$p < .05$ for indicated comparisons; two-way ANOVA with Holm-Sidak's multiple comparison test (B, E)

deposition), and synaptic loss. The correlation of these events with the induction of microglial MafB immunoreactivity suggests, but does not prove, a role for microglia in mediating the effects of systemic inflammation (i.e., orthopedic surgery) on synaptic integrity in these mice. Our findings are consistent with the model proposed by Yousef et al.[12] to explain the deleterious effects of aged plasma on microglia. In fact, this model posits pro-inflammatory cytokines present in the systemic milieu of aged mice (e.g., TNF-α and IL-1β)—the same ones induced systemically in our orthopedic surgery model[45,46]—upregulate VCAM-1 on BECs, leading to sustained inflammatory activity at the BBB interface and transmission of inflammatory signals from the inflamed endothelium to microglia[12] and by extension, microglial phagocytosis of hippocampal synapses. Although it can be hypothesized that URMC-099 may exert its effects peripherally leading to cerebrovascular dysfunction, we have previously shown that URMC-099 does not affect neutrophil expansion.[20] It can still be argued that URMC-099's therapeutic potential may act directly on modulating neutrophil activation and the release of NETs. Specifically, MLK3, one of the main targets of URMC-099, is responsible for neutrophil chemotaxis.[47] Nonetheless, we contend that URMC-099 exerts at least some of its therapeutic effects by inhibiting vascular signaling through leukocyte adhesion molecules (VCAM-1 and PECAM-1/CD31) and preservation of the BBB that would otherwise initiate the inflammatory cascade that leads to microgliosis and synaptic loss.

Systemic factors induce changes in microglial reactivity by multiple mechanisms. BECs relay systemic inflammatory signals to microglia *via* soluble factors[48,49] and direct microglial contacts with BECs.[50–53] In addition, breakdown of BEC tight junctions permits the direct entry of systemic factors (e.g., fibrinogen, systemic complement protein, etc.), many of which profoundly affect microglial function.[54,55] Finally, peripheral leukocytes can infiltrate the CNS and release inflammatory factors to nearby

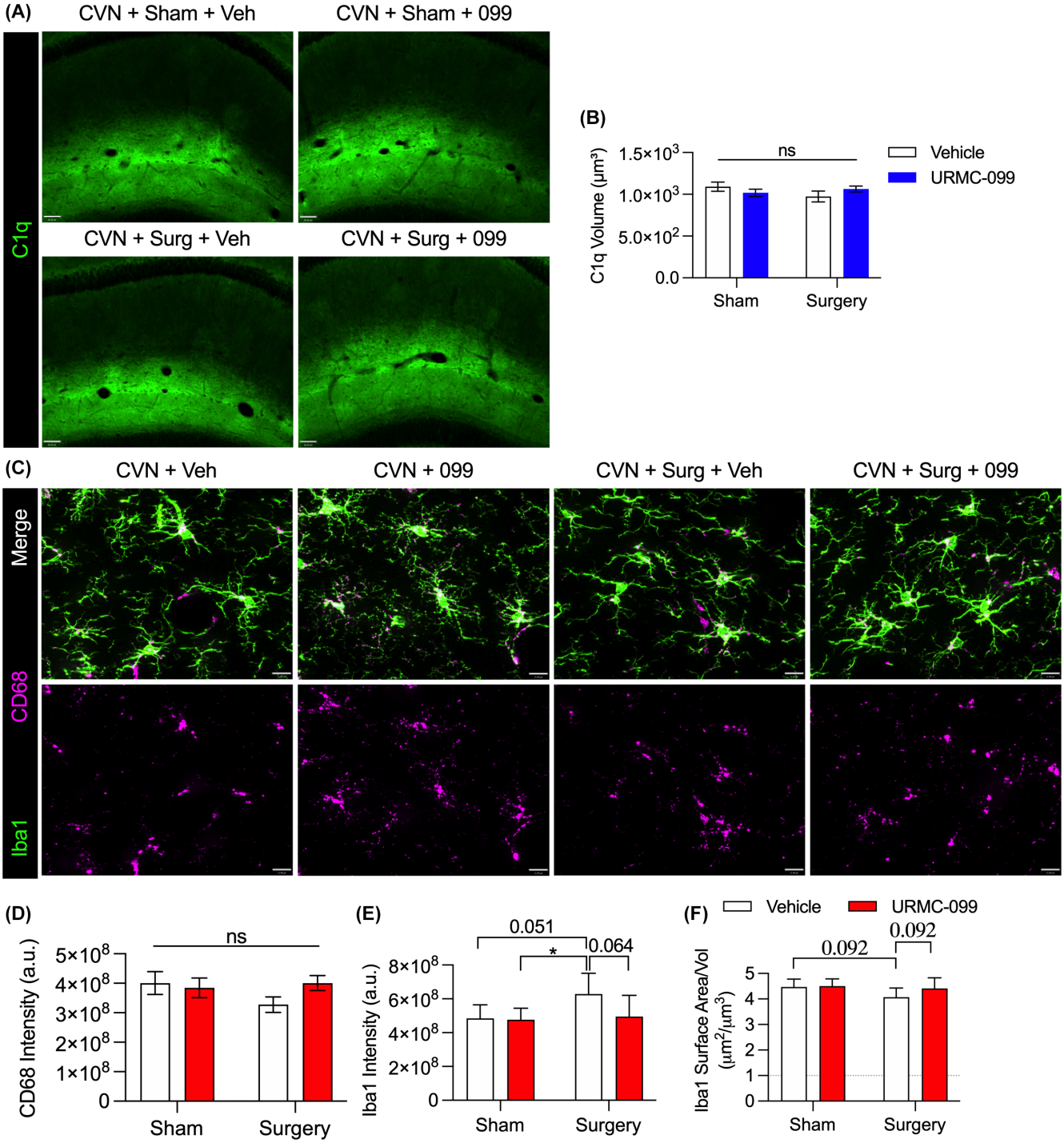

FIGURE 6 URMC-099 pretreatment does not change C1q or CD68 expression levels after surgery in the SLM of CVN-AD mice following orthopedic surgery. Six-month-old CVN-AD mice ($N = 6$/group) received three doses i.p. of URMC-099 (10 mg/kg) prior to undergoing sham or orthopedic surgery. (A) Representative image of C1q (green) localizing in the SLM; scale bar = 60 µm. (B) Quantification of C1q volume in the SLM. (C) Representative images depicting the pan-macrophage marker Iba1 (green), the lysosomal marker CD68 (magenta); scale bar = 11 µm. No effects were observed on CD68 expression (D), but surgery increased Iba-1 expression and decreased surface area with a trend in URMC-099-mediated decreases (E, F). Values presented as mean ± SEM ($N = 6$); *$p < .05$ for indicated comparisons; two-way ANOVA with Holm-Sidak's multiple comparison test (B–D)

cells. Indeed, CCR2+ monocytes infiltrate the hippocampal parenchyma *via* the choroid plexus following orthopedic surgery in mice.[56,57] In the present study, the vast majority (>95%) of SLM Iba1+ cells also expressed the microglia-specific marker Tmem119[58] (Figure S1), indicating that they were not peripherally derived. We believe

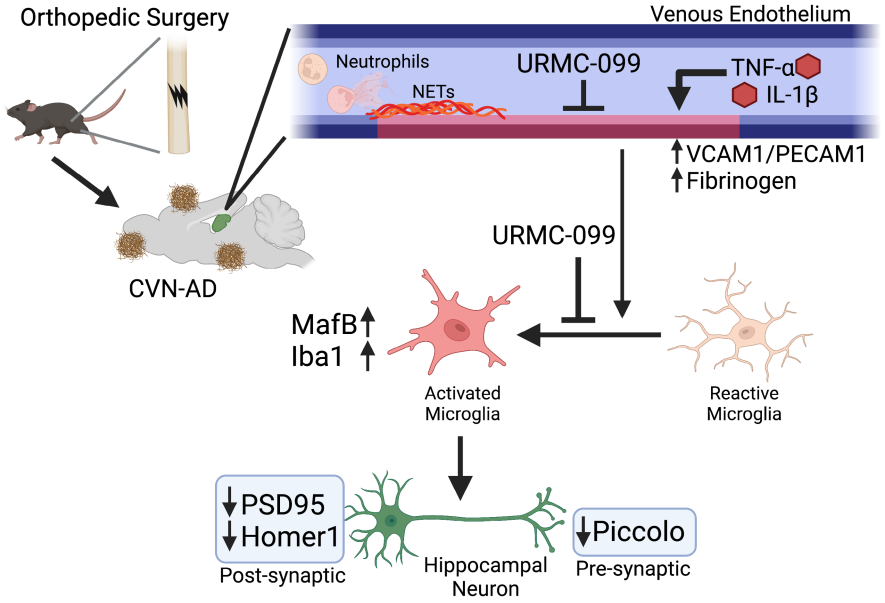

FIGURE 7 Proposed relationships between URMC-099 pretreatment and changes in endothelial, microglial, and synaptic markers following surgery in 6-month-old CVN-AD mice. Figure made in ©BioRender–biorender.com

the Tmem119-negative cells were either perivascular macrophages, which lack Tmem119 expression,[59] or reactive microglia that have downregulated their expression of this marker.[60] In addition, we did not observe any Ly6G+ neutrophils in the brain parenchyma. Based on our data, we conclude that the proinflammatory signals induced by orthopedic surgery are transmitted to microglia via an indirect mechanism that may involve leukocyte tethering to VCAM-1 but without leukocyte infiltration into the brain parenchyma. Prolonged tethering of proinflammatory leukocytes to vulnerable sites in the cerebrovasculature may be responsible for the pathological effects we observed, including damage to the BBB, loss of synaptic elements, and increased MafB immunoreactivity in SLM microglia, although the choreography of these cascading events remains unclear. Cellular and signaling intermediaries involved in these events, while beyond the scope of the present experiments, remain an active area of interest in future studies.

Microglia pathologically interact with synaptic elements in mouse models of neurodegeneration and neuroinflammation.[14,32,51,61,62] Because microglia mediate synapse loss in mouse models of AD *via* complement-dependent pruning processes,[32] and tibial fracture/fixation upregulated MafB, which in turn transcriptionally regulates C1q,[42] we investigated whether synapse loss in our DSD model might also depend on C1q. Here, we did not observe changes in C1q deposition or microglial CD68 immunoreactivity following orthopedic surgery in CVN-AD mice (Figure 6). It is worth noting, however, that C1q is deposited at high levels in the SLM of wild-type[43] and CVN-AD mice (this study). Moreover, we observed high levels of CD68 selectively in SLM microglia compared to surrounding regions across all our conditions. Thus, these two factors may predispose the SLM of CVN-AD mice to synaptic loss following systemic and/or CNS inflammation. We cannot discount the possibility that synaptic loss may be due to fibrinogen leakage. In the context of AD, fibrinogen has been shown to bind to CD11b causing synaptic pruning independent of amyloid plaques.[55] We cannot completely exclude the possibility that our synaptic data reflect changes in the expression of genes encoding Piccolo, PSD95, and Homer1, as has been observed in AD patients,[63] or the clustering of these proteins in synaptic structures (that would influence their ability to form punctae). Even so, changes in synaptic gene expression correlate with cognitive impairment in AD patients,[64,65] and microglial depletion ameliorates pathological changes in synaptic gene expression in mouse AD models.[66] Notwithstanding these possibilities, we believe our results are most consistent with a synaptic engulfment mechanism because MafB has been shown to be upregulated in macrophage following efferocytosis in vitro[42] and in neurodegenerative contexts like peripheral nerve injury[35]; thus, we interpret microglial MafB induction as a sign of synaptic engulfment. Corroboration of MafB-mediated synaptic engulfment at the nanoscale level, while beyond the scope of these experiments, remains topic of investigation in future studies. Thus, we believe the amelioration of synaptic loss we observed in our model of DSD is likely dependent on microglia, which are tractable targets for URMC-099 prophylaxis in protecting the neurovascular unit from postoperative complications including delirium and dementia.

Overall, we demonstrated that orthopedic surgery perturbs the BBB, induces microgliosis, and causes synaptic damage in 6-month-old CVN mice; furthermore, we showed that URMC-099 prophylaxis abrogates these

pathological effects. Based on these findings, we conclude that our therapeutic approach may significantly decrease the deleterious effects of DSD in the elderly population at risk for morbidity and mortality after surgery.

AUTHOR CONTRIBUTIONS

Patrick Miller-Rhodes performed the experiments, analyzed the data, and wrote and edited the manuscript. Herman Li performed the experiments, analyzed the data, and wrote and edited the manuscript. Ravikanth Velagapudi performed experiments on CVN-AD mice. Wesley Chiang performed experiments on bEND.3 cells. Niccolò Terrando and Harris A. Gelbard supervised Patrick Miller-Rhodes and Herman Li and contributed to the interpretation of the data.

ACKNOWLEDGEMENTS

We thank Angela Stout in the Gelbard lab for her technical expertise.

DISCLOSURES

Niccolò Terrando is in the scientific advisory board of Pioneura Corp.; Harris A. Gelbard is the chief science officer of Pioneura Corp. Pioneura Corp. holds the exclusive license for the development of URMC-099, but contributed no funding or financial support to Drs. Terrando and Gelbard for this work.

ETHICS APPROVAL

The procedures followed to provide tissues from APPSwDI/mNos2$^{-/-}$ (CVN-AD) mice were performed in strict compliance with animal protocols approved by the Institutional Animal Care and Use Committees (IACUC) of Duke University (A249-17-11).

CONSENT FOR PUBLICATION

All authors have reviewed the data and its interpretation and consent to the submission of this publication.

DATA AVAILABILITY STATEMENT

All data generated or analyzed during this study are included in this published article and its supplementary information files.

ORCID

Niccolò Terrando https://orcid.org/0000-0003-1803-5853

REFERENCES

1. Schulman-Green D, Hshieh T, Adamis D, et al. Domains of delirium severity in Alzheimer's disease and related dementias. *J Am Geriatr Soc*. 2021. doi:10.1111/jgs.17624. Epub ahead of print.
2. Elie M, Cole MG, Primeau FJ, et al. Delirium risk factors in elderly hospitalized patients. *J Gen Intern Med*. 1998;13(3):204-212.
3. Lee HB, Oldham MA, Sieber FE, et al. Impact of delirium after hip fracture surgery on one-year mortality in patients with or without dementia: a case of effect modification. *Am J Geriatr Psychiatry*. 2017;25(3):308-315.
4. Wilson JE, Mart MF, Cunningham C, et al. Delirium. *Nat Rev Dis Primers*. 2020;6(1):90.
5. Fong TG, Davis D, Growdon ME, et al. The interface between delirium and dementia in elderly adults. *Lancet Neurol*. 2015;14(8):823-832.
6. Davis DHJ, Muniz Terrera G, Keage H, et al. Delirium is a strong risk factor for dementia in the oldest-old: a population-based cohort study. *Brain*. 2012;135(Pt 9):2809-2816.
7. Wang P, Velagapudi R, Kong C, et al. Neurovascular and immune mechanisms that regulate postoperative delirium superimposed on dementia. *Alzheimers Dement*. 2020;16(5):734-749.
8. Kan MJ, Lee JE, Wilson JG, et al. Arginine deprivation and immune suppression in a mouse model of Alzheimer's disease. *J Neurosci*. 2015;35(15):5969-5982.
9. Hoos MD, Richardson BM, Foster MW, et al. Longitudinal study of differential protein expression in an Alzheimer's mouse model lacking inducible nitric oxide synthase. *J Proteome Res*. 2013;12(10):4462-4477.
10. Colton CA, Wilson JG, Everhart A, et al. mNos2 deletion and human NOS2 replacement in Alzheimer disease models. *J Neuropathol Exp Neurol*. 2014;73(8):752-769.
11. Wilcock DM, Lewis MR, Van Nostrand WE, et al. Progression of amyloid pathology to Alzheimer's disease pathology in an amyloid precursor protein transgenic mouse model by removal of nitric oxide synthase 2. *J Neurosci*. 2008;28(7):1537-1545.
12. Yousef H, Czupalla CJ, Lee D, et al. Aged blood impairs hippocampal neural precursor activity and activates microglia via brain endothelial cell VCAM1. *Nat Med*. 2019;25(6):988-1000.
13. Goodfellow VS, Loweth CJ, Ravula SB, et al. Discovery, synthesis, and characterization of an orally bioavailable, brain penetrant inhibitor of mixed lineage kinase 3. *J Med Chem*. 2013;56(20):8032-8048.
14. Bellizzi MJ, Hammond JW, Li H, et al. The mixed-lineage kinase inhibitor URMC-099 protects hippocampal synapses in experimental autoimmune encephalomyelitis. *eNeuro*. 2018;5(6):1-14.
15. Dong W, Embury CM, Lu Y, et al. The mixed-lineage kinase 3 inhibitor URMC-099 facilitates microglial amyloid-beta degradation. *J Neuroinflammation*. 2016;13(1):184.
16. Kiyota T, Machhi J, Lu Y, et al. URMC-099 facilitates amyloid-beta clearance in a murine model of Alzheimer's disease. *J Neuroinflammation*. 2018;15(1):137.
17. Tomita K, Kohli R, MacLaurin BL, et al. Mixed-lineage kinase 3 pharmacological inhibition attenuates murine nonalcoholic steatohepatitis. *JCI Insight*. 2017;2(15):94488.
18. Puccini JM, Marker DF, Fitzgerald T, et al. Leucine-rich repeat kinase 2 modulates neuroinflammation and neurotoxicity in models of human immunodeficiency virus 1-associated neurocognitive disorders. *J Neurosci*. 2015;35(13):5271-5283.
19. Bos PH, Lowry ER, Costa J, et al. Development of MAP4 kinase inhibitors as motor neuron-protecting agents. *Cell Chem Biol*. 2019;26(12):1703-1715.e37.
20. Miller-Rhodes P, Kong C, Baht GS, et al. The broad spectrum mixed-lineage kinase 3 inhibitor URMC-099 prevents acute microgliosis and cognitive decline in a mouse model of perioperative neurocognitive disorders. *J Neuroinflammation*. 2019;16(1):193.

21. Montesano R, Pepper MS, Möhle-Steinlein U, et al. Increased proteolytic activity is responsible for the aberrant morphogenetic behavior of endothelial cells expressing the middle T oncogene. *Cell*. 1990;62(3):435-445.
22. Glynn MW, McAllister AK. Immunocytochemistry and quantification of protein colocalization in cultured neurons. *Nat Protoc*. 2006;1(3):1287-1296.
23. Munji RN, Soung AL, Weiner GA, et al. Profiling the mouse brain endothelial transcriptome in health and disease models reveals a core blood-brain barrier dysfunction module. *Nat Neurosci*. 2019;22(11):1892-1902.
24. Suzuki H, Hasegawa YU, Kanamaru K, et al. Mechanisms of osteopontin-induced stabilization of blood-brain barrier disruption after subarachnoid hemorrhage in rats. *Stroke*. 2010;41(8):1783-1790.
25. Tang J, Kang Y, Huang L, et al. TIMP1 preserves the blood-brain barrier through interacting with CD63/integrin β 1 complex and regulating downstream FAK/RhoA signaling. *Acta Pharm Sin B*. 2020;10(6):987-1003.
26. Thomsen MS, Birkelund S, Burkhart A, et al. Synthesis and deposition of basement membrane proteins by primary brain capillary endothelial cells in a murine model of the blood-brain barrier. *J Neurochem*. 2017;140(5):741-754.
27. Cavallari M, Dai W, Guttmann CRG, et al. Neural substrates of vulnerability to postsurgical delirium as revealed by presurgical diffusion MRI. *Brain*. 2016;139(Pt 4):1282-1294.
28. Yang X, Yao C, Tian T, et al. A novel mechanism of memory loss in Alzheimer's disease mice via the degeneration of entorhinal-CA1 synapses. *Mol Psychiatry*. 2018;23(2):199-210.
29. Shen Z, Lu Z, Chhatbar PY, et al. An artery-specific fluorescent dye for studying neurovascular coupling. *Nat Methods*. 2012;9(3):273-276.
30. Gustavsson C, Agardh C-D, Zetterqvist AV, et al. Vascular cellular adhesion molecule-1 (VCAM-1) expression in mice retinal vessels is affected by both hyperglycemia and hyperlipidemia. *PLoS One*. 2010;5(9):e12699.
31. Terrando N, Gómez-Galán M, Yang T, et al. Aspirin-triggered resolvin D1 prevents surgery-induced cognitive decline. *FASEB J*. 2013;27(9):3564-3571.
32. Hong S, Beja-Glasser VF, Nfonoyim BM, et al. Complement and microglia mediate early synapse loss in Alzheimer mouse models. *Science*. 2016;352(6286):712-716.
33. Femenía T, Giménez-Cassina A, Codeluppi S, et al. Disrupted neuroglial metabolic coupling after peripheral surgery. *J Neurosci*. 2018;38(2):452-464.
34. Crotti A, Benner C, Kerman BE, et al. Mutant Huntingtin promotes autonomous microglia activation via myeloid lineage-determining factors. *Nat Neurosci*. 2014;17(4):513-521.
35. Tozaki-Saitoh H, Masuda J, Kawada R, et al. Transcription factor MafB contributes to the activation of spinal microglia underlying neuropathic pain development. *Glia*. 2019;67(4):729-740.
36. Miller-Rhodes P, Gelbard HA. The cell culture environment regulates the transcription factor MafB in BV-2 microglia. *Matters (Zur)*. 2021;2021:1-13.
37. Pfrieger FW. Role of cholesterol in synapse formation and function. *Biochim Biophys Acta*. 2003;1610(2):271-280.
38. Bennett ML, Bennett FC, Liddelow SA, et al. New tools for studying microglia in the mouse and human CNS. *Proc Natl Acad Sci U S A*. 2016;113(12):E1738-E1746.
39. Yu W-M, Appler JM, Kim Y-H, et al. A Gata3-Mafb transcriptional network directs post-synaptic differentiation in synapses specialized for hearing. *eLife*. 2013;2:e01341.
40. Pai E-L, Vogt D, Clemente-Perez A, et al. Mafb and c-Maf have prenatal compensatory and postnatal antagonistic roles in cortical interneuron fate and function. *Cell Rep*. 2019;26(5):1157-1173.e5.
41. Bialas AR, Stevens B. TGF-β signaling regulates neuronal C1q expression and developmental synaptic refinement. *Nat Neurosci*. 2013;16(12):1773-1782.
42. Tran MTN, Hamada M, Jeon H, et al. MafB is a critical regulator of complement component C1q. *Nat Commun*. 2017;8(1):1700.
43. Stephan AH, Madison DV, Mateos JM, et al. A dramatic increase of C1q protein in the CNS during normal aging. *J Neurosci*. 2013;33(33):13460-13474.
44. Hendrickx DAE, van Eden CG, Schuurman KG, et al. Staining of HLA-DR, Iba1 and CD68 in human microglia reveals partially overlapping expression depending on cellular morphology and pathology. *J Neuroimmunol*. 2017;309:12-22.
45. Cibelli M, Fidalgo AR, Terrando N, et al. Role of interleukin-1beta in postoperative cognitive dysfunction. *Ann Neurol*. 2010;68(3):360-368.
46. Terrando N, Monaco C, Ma D, Foxwell BM, Feldmann M, Maze M. Tumor necrosis factor-alpha triggers a cytokine cascade yielding postoperative cognitive decline. *Proc Natl Acad Sci U S A*. 2010;107(47):20518-20522.
47. Polesskaya O, Wong C, Lebron L, et al. MLK3 regulates fMLP-stimulated neutrophil motility. *Mol Immunol*. 2014;58(2):214-222.
48. Liu X, Nemeth DP, McKim DB, et al. Cell-type-specific interleukin 1 receptor 1 signaling in the brain regulates distinct neuroimmune activities. *Immunity*. 2019;50(2):317-333.e6.
49. Zhu L, Liu X, Nemeth DP, et al. Interleukin-1 causes CNS inflammatory cytokine expression via endothelia-microglia bi-cellular signaling. *Brain Behav Immun*. 2019;81:292-304.
50. Lassmann H, Zimprich F, Vass K, et al. Microglial cells are a component of the perivascular glia limitans. *J Neurosci Res*. 1991;28(2):236-243.
51. Bisht K, Sharma KP, Lecours C, et al. Dark microglia: a new phenotype predominantly associated with pathological states. *Glia*. 2016;64(5):826-839.
52. Lou N, Takano T, Pei Y, et al. Purinergic receptor P2RY12-dependent microglial closure of the injured blood-brain barrier. *Proc Natl Acad Sci U S A*. 2016;113(4):1074-1079.
53. Joost E, Jordão MJC, Mages B, et al. Microglia contribute to the glia limitans around arteries, capillaries and veins under physiological conditions, in a model of neuroinflammation and in human brain tissue. *Brain Struct Funct*. 2019;224(3):1301-1314.
54. Bohlen CJ, Bennett FC, Tucker AF, et al. Diverse requirements for microglial survival, specification, and function revealed by defined-medium cultures. *Neuron*. 2017;94(4):759-773.e8.
55. Merlini M, Rafalski VA, Rios Coronado PE, et al. Fibrinogen induces microglia-mediated spine elimination and cognitive impairment in an Alzheimer's disease model. *Neuron*. 2019;101(6):1099-1108.e6.
56. Terrando N, Eriksson LI, Kyu Ryu J, et al. Resolving postoperative neuroinflammation and cognitive decline. *Ann Neurol*. 2011;70(6):986-995.

57. Feng X, Valdearcos M, Uchida Y, et al. Microglia mediate postoperative hippocampal inflammation and cognitive decline in mice. *JCI Insight*. 2017;2(7):e91229.
58. Bennett FC, Bennett ML, Yaqoob F, et al. A combination of ontogeny and CNS environment establishes microglial identity. *Neuron*. 2018;98(6):1170-1183.e8.
59. Goldmann T, Wieghofer P, Jordão MJC, et al. Origin, fate and dynamics of macrophages at central nervous system interfaces. *Nat Immunol*. 2016;17(7):797-805.
60. Krasemann S, Madore C, Cialic R, et al. The TREM2-APOE pathway drives the transcriptional phenotype of dysfunctional microglia in neurodegenerative diseases. *Immunity*. 2017;47(3):566-581.e9.
61. Marker DF, Tremblay M-E, Puccini JM, et al. The new small-molecule mixed-lineage kinase 3 inhibitor URMC-099 is neuroprotective and anti-inflammatory in models of human immunodeficiency virus-associated neurocognitive disorders. *J Neurosci*. 2013;33(24):9998-10010.
62. Savage JC, St-Pierre MK, Hui CW, Tremblay M-E. Microglial ultrastructure in the hippocampus of a lipopolysaccharide-induced sickness mouse model. *Front Neurosci*. 2019;13:1340.
63. Tucsek Z, Noa Valcarcel-Ares M, Tarantini S, et al. Hypertension-induced synapse loss and impairment in synaptic plasticity in the mouse hippocampus mimics the aging phenotype: implications for the pathogenesis of vascular cognitive impairment. *Geroscience*. 2017;39(4):385-406.
64. Honer WG. Pathology of presynaptic proteins in Alzheimer's disease: more than simple loss of terminals. *Neurobiol Aging*. 2003;24(8):1047-1062.
65. Counts SE, Alldred MJ, Che S, et al. Synaptic gene dysregulation within hippocampal CA1 pyramidal neurons in mild cognitive impairment. *Neuropharmacology*. 2014;79:172-179.
66. Spangenberg E, Severson PL, Hohsfield LA, et al. Sustained microglial depletion with CSF1R inhibitor impairs parenchymal plaque development in an Alzheimer's disease model. *Nat Commun*. 2019;10(1):3758.

SUPPORTING INFORMATION

Additional supporting information may be found in the online version of the article at the publisher's website.

How to cite this article: Miller-Rhodes P, Li H, Velagapudi R, Chiang W, Terrando N, Gelbard HA. URMC-099 prophylaxis prevents hippocampal vascular vulnerability and synaptic damage in an orthopedic model of delirium superimposed on dementia. *FASEB J*. 2022;36:e22343. doi:10.1096/fj.202200184RR